Supplementary Information

Stable organic electrochemical neurons based on p-type and n-type ladder polymers

Han-Yan Wu,[a#] Jun-Da Huang,[ab#] Sang Young Jeong,[c] Tiefeng Liu,[a] Ziang Wu,[c] Tom van der Pol,[a] Qingqing Wang,[a] Marc-Antoine Stoeckel,[ab] Qifan Li,[a] Mats Fahlman,[a] Deyu Tu,[a] Han Young Woo,[c] Chi-Yuan Yang,[ab] and Simone Fabiano[ab]*

[a]Laboratory of Organic Electronics, Department of Science and Technology, Linköping University, SE-60174 Norrköping, Sweden
[b]n-Ink AB, Bredgatan 33, SE-60221 Norrköping, Sweden
[c]Department of Chemistry, College of Science, Korea University, Seoul 136-713, Republic of Korea

E-mail: simone.fabiano@liu.se

Table of contents

Author contributions
Figures S1-S28
Tables S1-S2

Author contributions:
H.-Y.W. and J.-D. H. contributed equally to this work. J.-D.H. synthesized the materials. H.-Y.W. prepared samples and measured absorption spectroscopy, CV, spectroelectrochemistry, DLS, EIS, OECTs, inverters, and LIF neurons. S.Y.J., Z. W., H.Y.Woo, and C.Y.Y. measured and analyzed the GIWAXS data. T.L. helped with spectroscopy measurements. T. van der P. carried out the FTIR measurement. Q.W. and M. F. measured XPS and analyzed the data. M.-A. S. performed AFM measurements. Q.L. assisted with OECT sample fabrication. C.-Y.Y. initiated the project. S.F. and C.-Y. Y. designed and supervised the experiments. H.-Y.W., C.-Y.Y., D.T., and S.F. wrote the manuscript. All authors contributed to discussion and manuscript preparation.

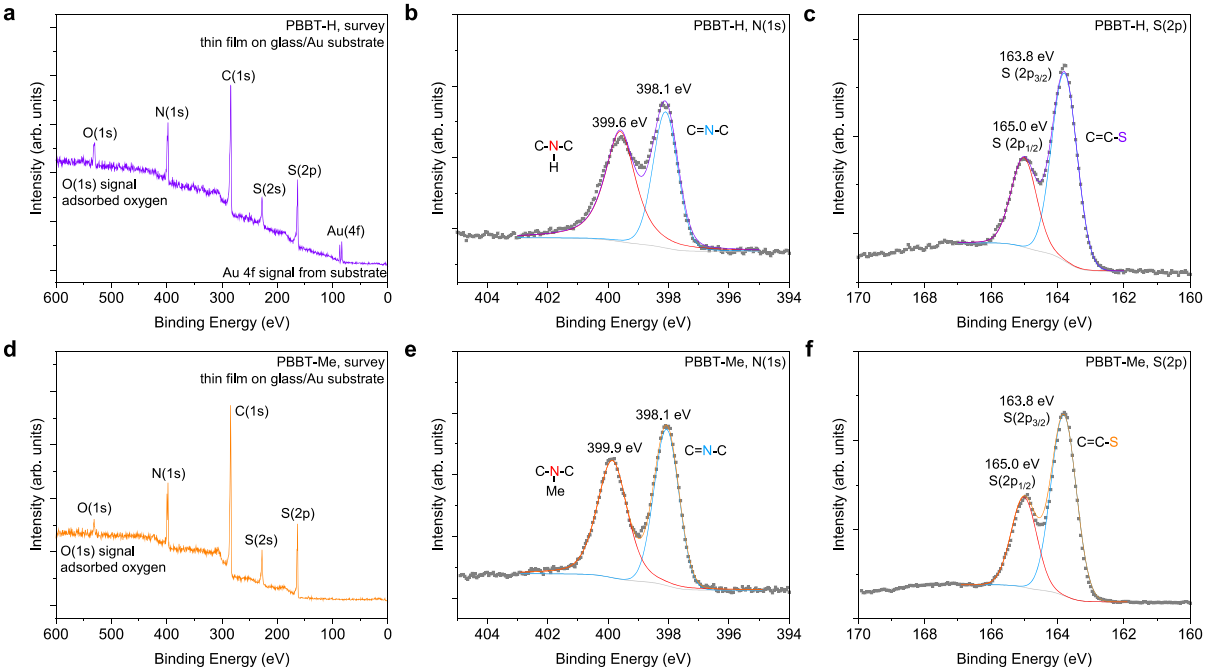

Fig. S1. X-ray photoelectron spectroscopy (XPS) analysis of PBBT-H (a-c) and PBBT-Me (d-e). The N(1s) and S(2p) peaks potion of PBBT-H is in agreement with previous results (ref. 1). The N(1s) signal relative to the N atom in the pyrrole unit (399.6 eV, PBBT-H) shifts to a higher binding energy (399.9 eV, PBBT-H) due to higher electronegativity of the C atom in PBBT-Me compared to the H atom in PBBT-H.

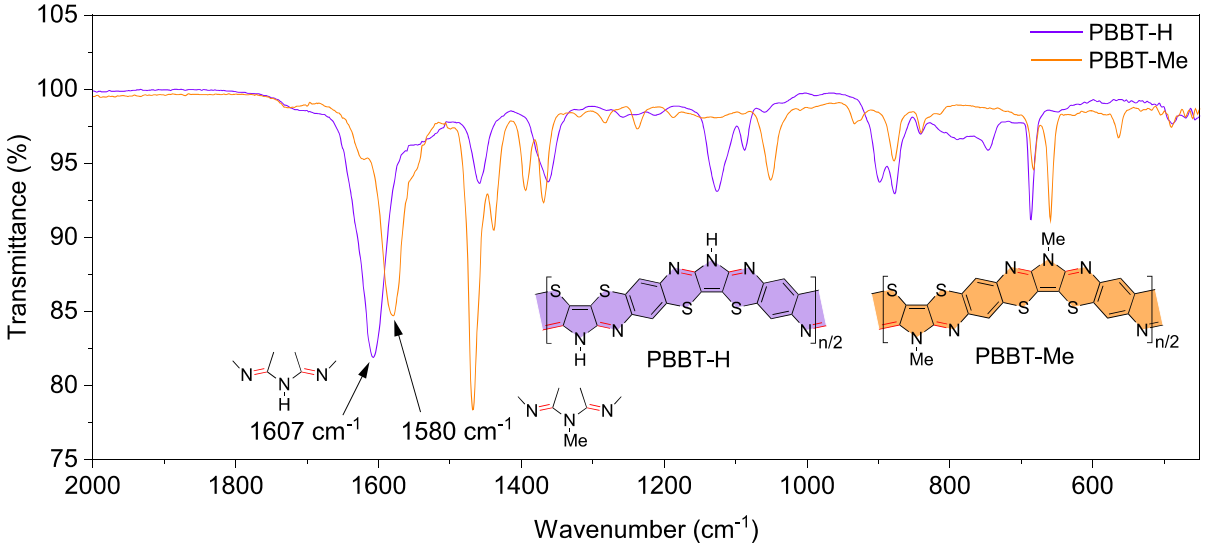

Fig. S2. Fourier-transform infrared (FTIR) spectra of PBBT-H and PBBT-Me. The FTIR spectrum of PBBT-H is consistent with previous results (ref. 2). The peak at 1607 cm^{-1} of the PBBT-H's FTIR spectrum is ascribed to the N=C bond vibration. The inductive effect of the CH_3– group in PBBT-Me shifts to the peak position at lower wavenumbers (1580 cm^{-1}) due to the lowering of the N=C bond strength.

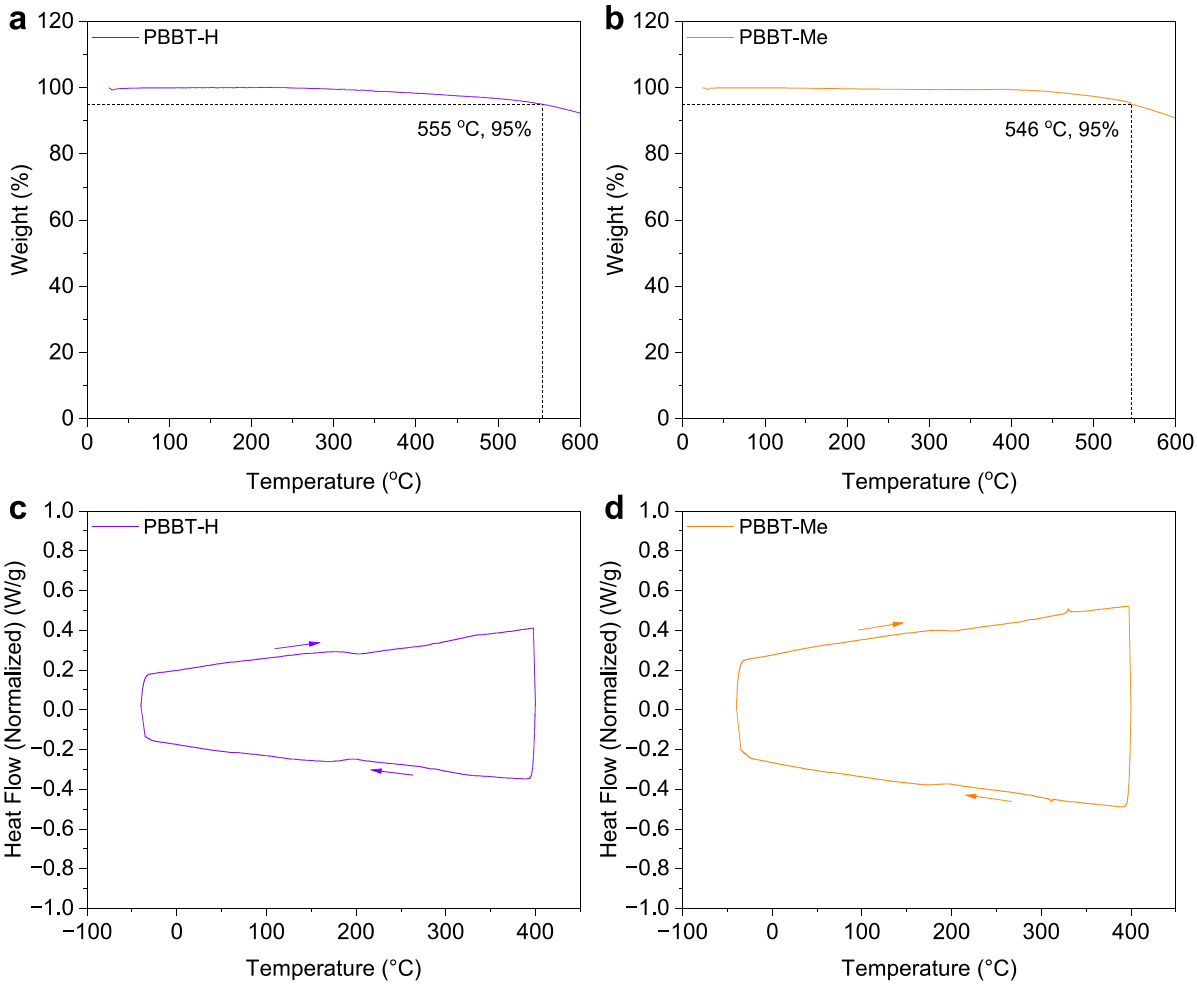

Fig. S3. a-b) Thermogravimetric analysis of PBBT-H (a) and PBBT-Me (b). Netzsch STA449C was used to perform TGA. 5.00 mg of each polymer was heated from 25 °C to 600 °C at a heating rate of 10 °C/min under argon purging. The polymers' decomposition temperatures are reported. c-d) Differential scanning calorimetry of PBBT-H (c) and PBBT-Me (d). TA Instruments Discovery DSC 250 was used to perform DSC. 5.00 mg of each polymer was heated and cooled between -40 °C and 400 °C at a heating rate of 20 °C/min.

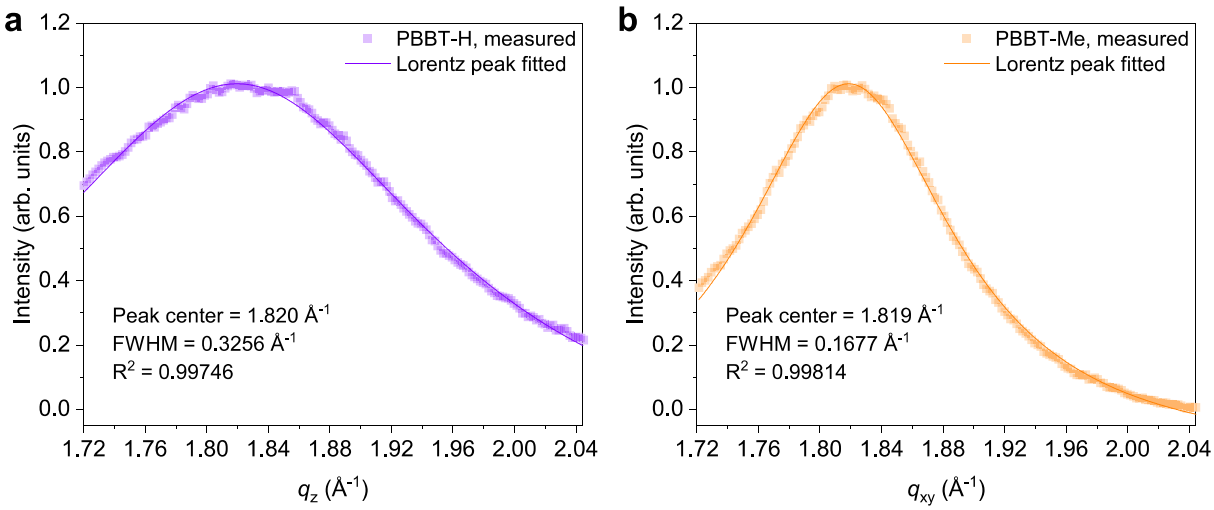

Fig. S4. GIWAXS analysis: π-π stacking (010) diffraction analysis of PBBT-H (a) and PBBT-Me (b).

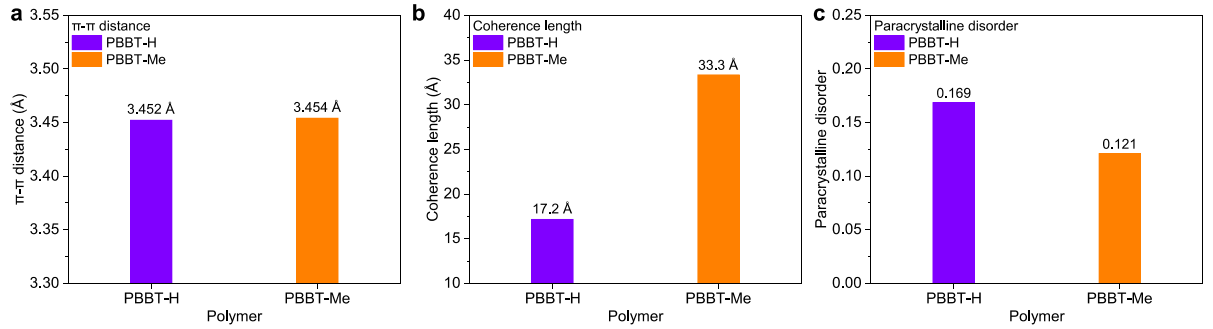

Fig. S5. GIWAXS analysis: a) π-π distance ($d_{\pi\text{-}\pi}$) of PBBT-H and PBBT-Me. b) Coherence length ($L_{c(010)}$) of PBBT-H and PBBT-Me. (c) Paracrystalline disorder ($g_{(010)}$) of PBBT-H and PBBT-Me.

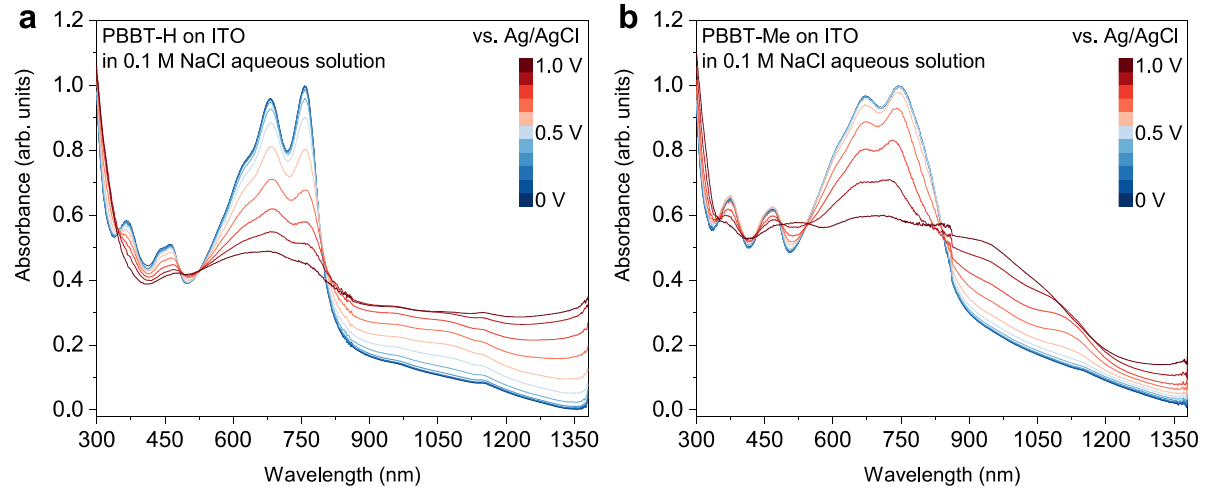

Fig. S6. Spectroelectrochemistry: Original absorption spectra of PBBT-H (a) and PBBT-Me (b) scanned between 0 V and 1.0 V versus Ag/AgCl in 0.1 M NaCl aqueous solution. The Ag/AgCl electrode was grounded and the bias voltage was applied to the polymer films.

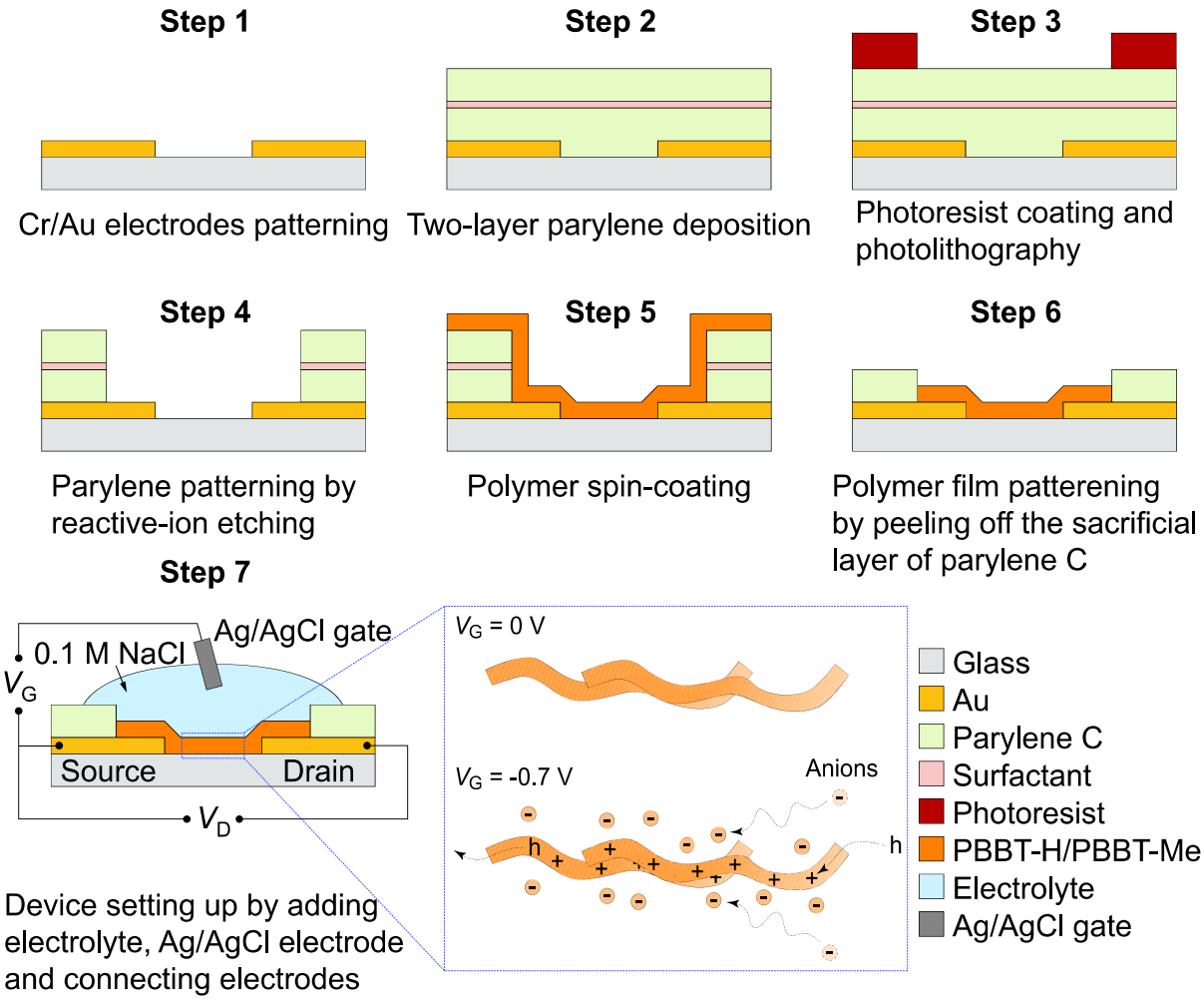

Fig. S7. Schematic of structure, preparation process, and operation mechanism of OECTs.

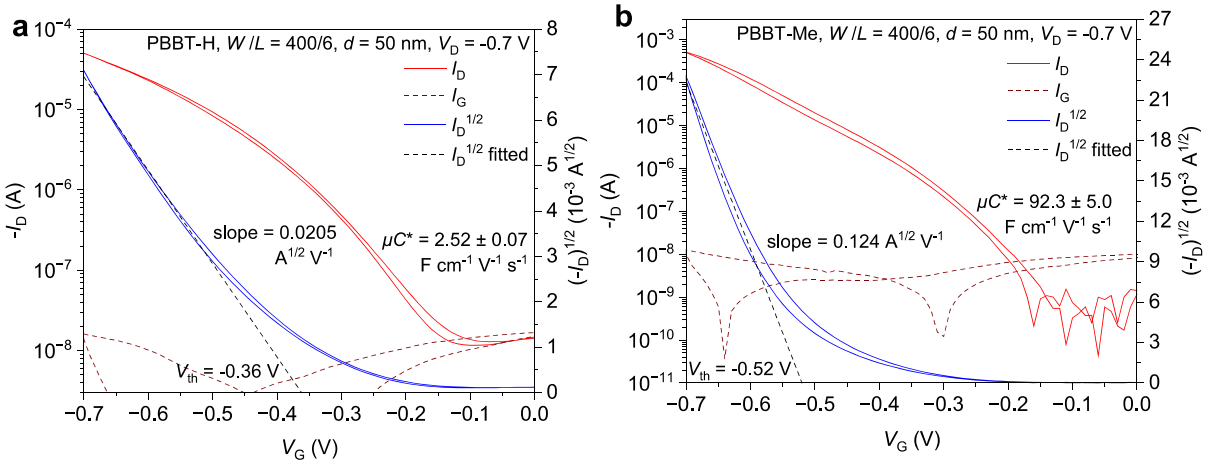

Fig. S8. OECT performance: Transfer curves of PBBT-H (a) and PBBT-Me (b). The drain current (I_D), the gate current (I_G), the square root of I_D ($I_D^{1/2}$), the fitted threshold voltage V_{th} and the μC^* were reported.

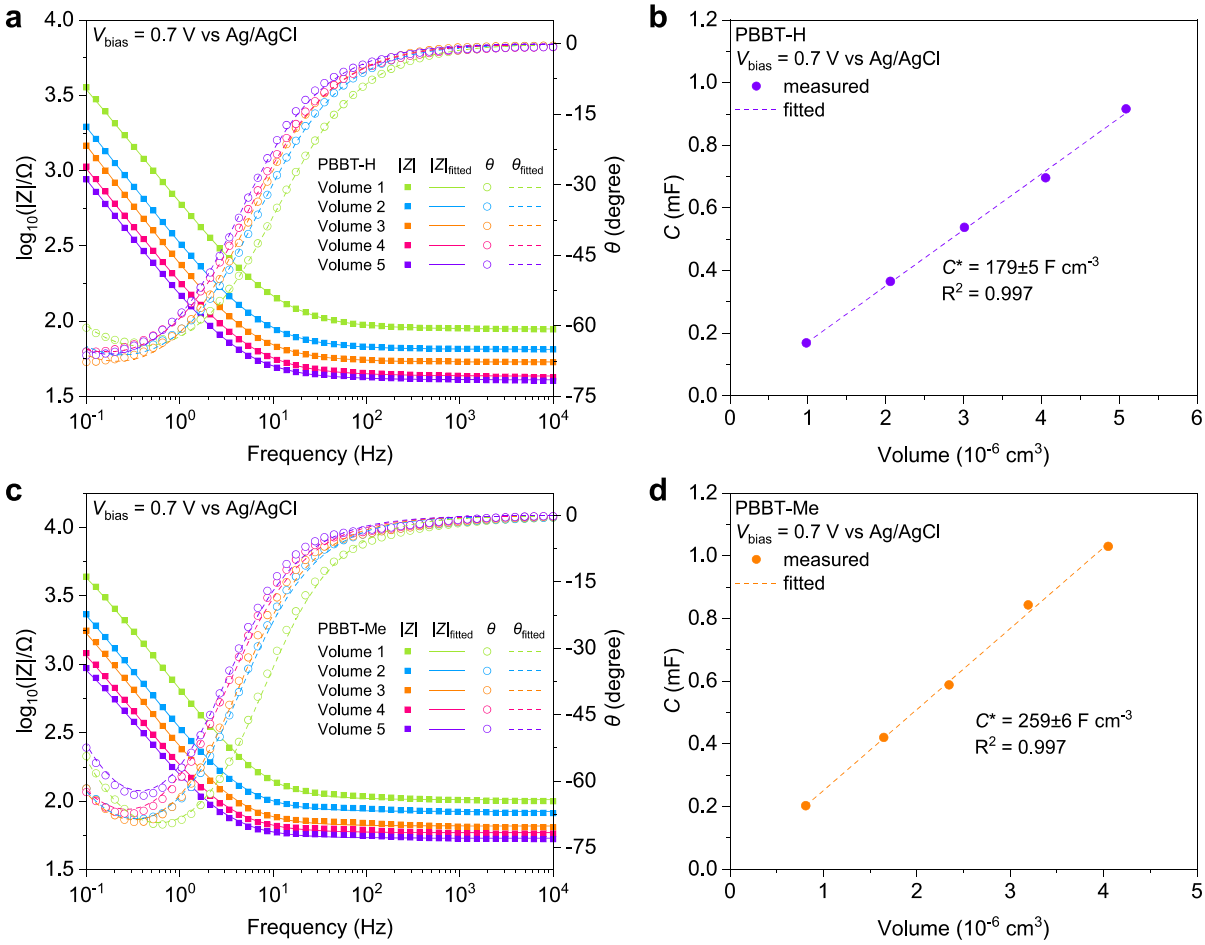

Fig. S9. Electrochemical impedance spectroscopy and volumetric capacitance at the voltage bias (V_{bias}) of 0.7 V: a,c) Bode impedance of PBBT-H (a) and PBBT-Me (c). b,d) Fitted capacitance versus volume of PBBT-H (b) and PBBT-Me (d) thin films. The measurement and fitting are described in the Experiment Section.

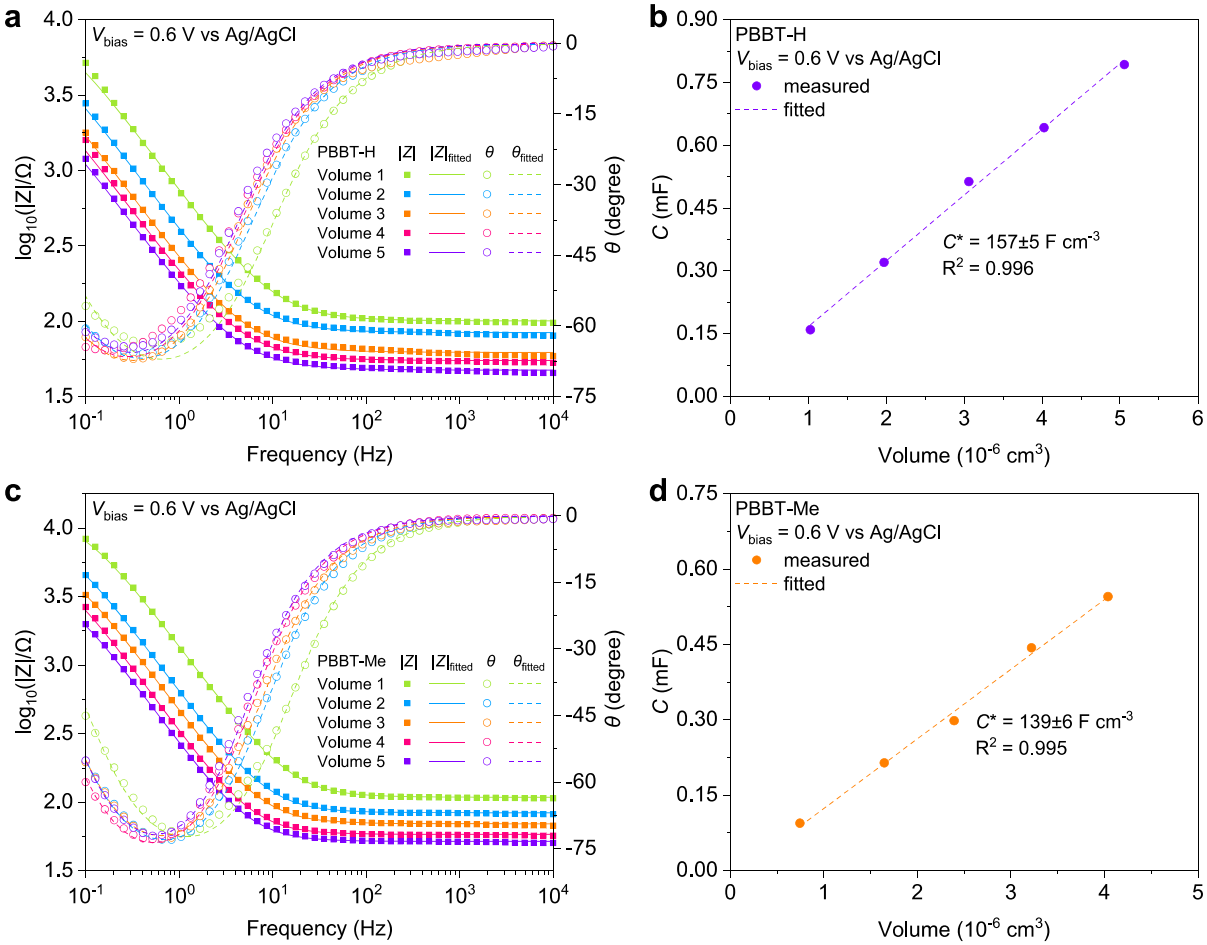

Fig. S10. Electrochemical impedance spectroscopy and volumetric capacitance at the voltage bias (V_{bias}) of 0.6 V: a,c) Bode impedance of PBBT-H (a) and PBBT-Me (c). b,d) Fitted capacitance versus volume of PBBT-H (b) and PBBT-Me (d) thin films. The measurement and fitting are described in the Experiment Section.

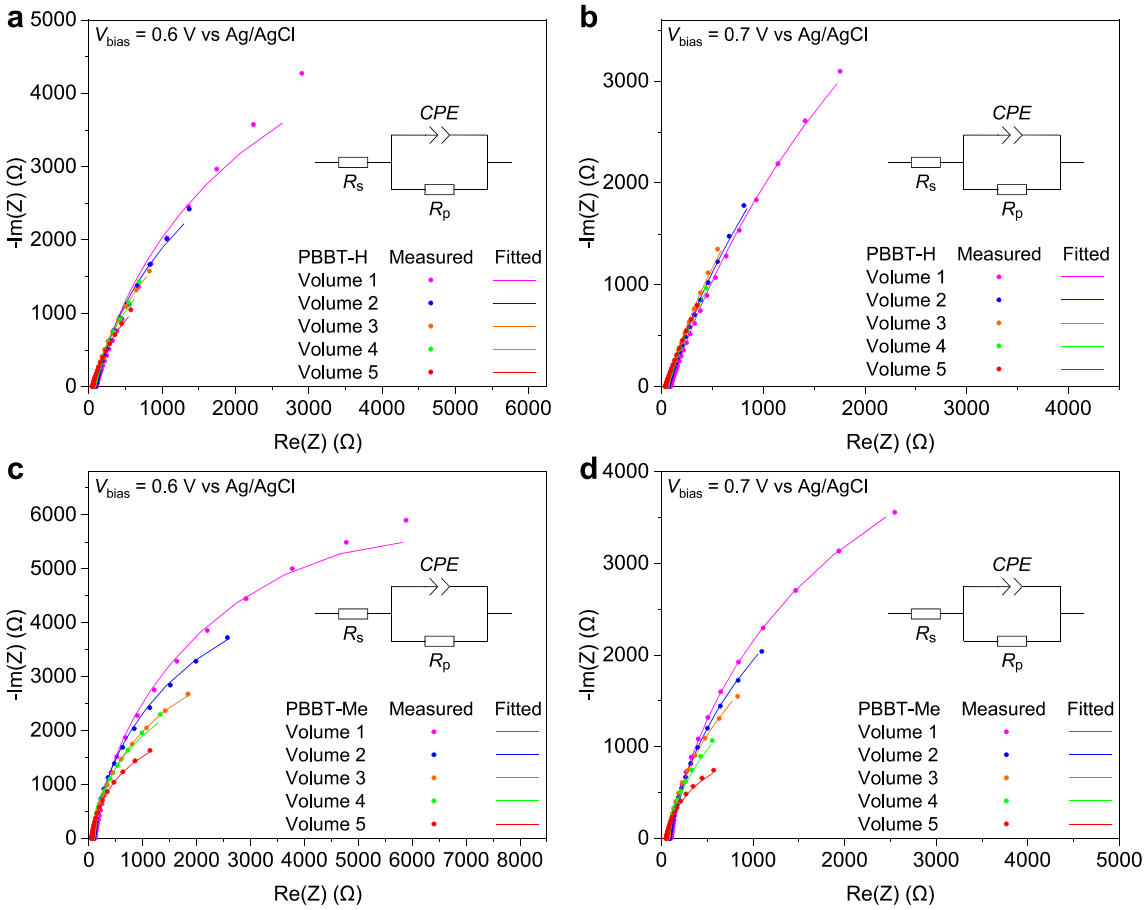

Fig. S11. Nyquist impedance and fitted curves of PBBT-H at voltage bias (V_{bias}) of 0.6 V (a) and 0.7 V (b), and PBBT-Me at V_{bias} of 0.6 V (c) and 0.7 V (d). These plots show that the measured data conform well to the classical Randles circuit model, represented as $R_s(R_p||CPE)$. Importantly, the Nyquist impedance plots observed for PBBT-H and PBBT-Me are consistent with those typically observed for other organic mixed ionic-electronic conductors (refs. 3, 4).

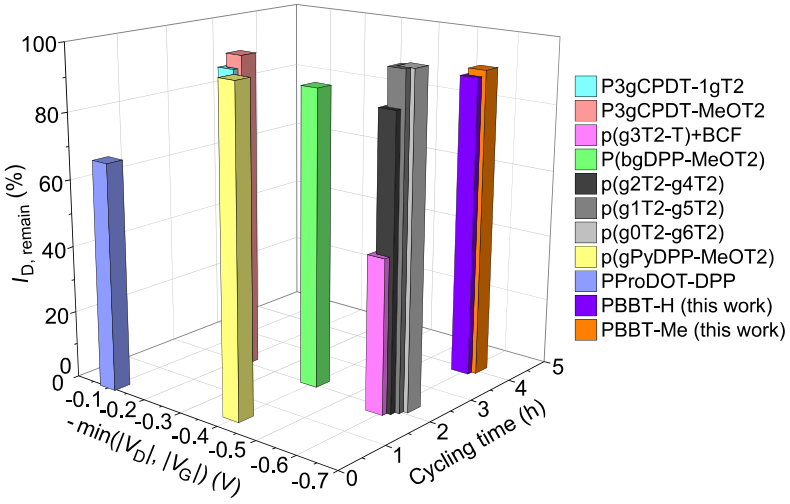

Fig. S12. Comparison of p-type, accumulation mode OECT stability under continuous cycling in air with aqueous solution electrolyte. Data from Table S1.

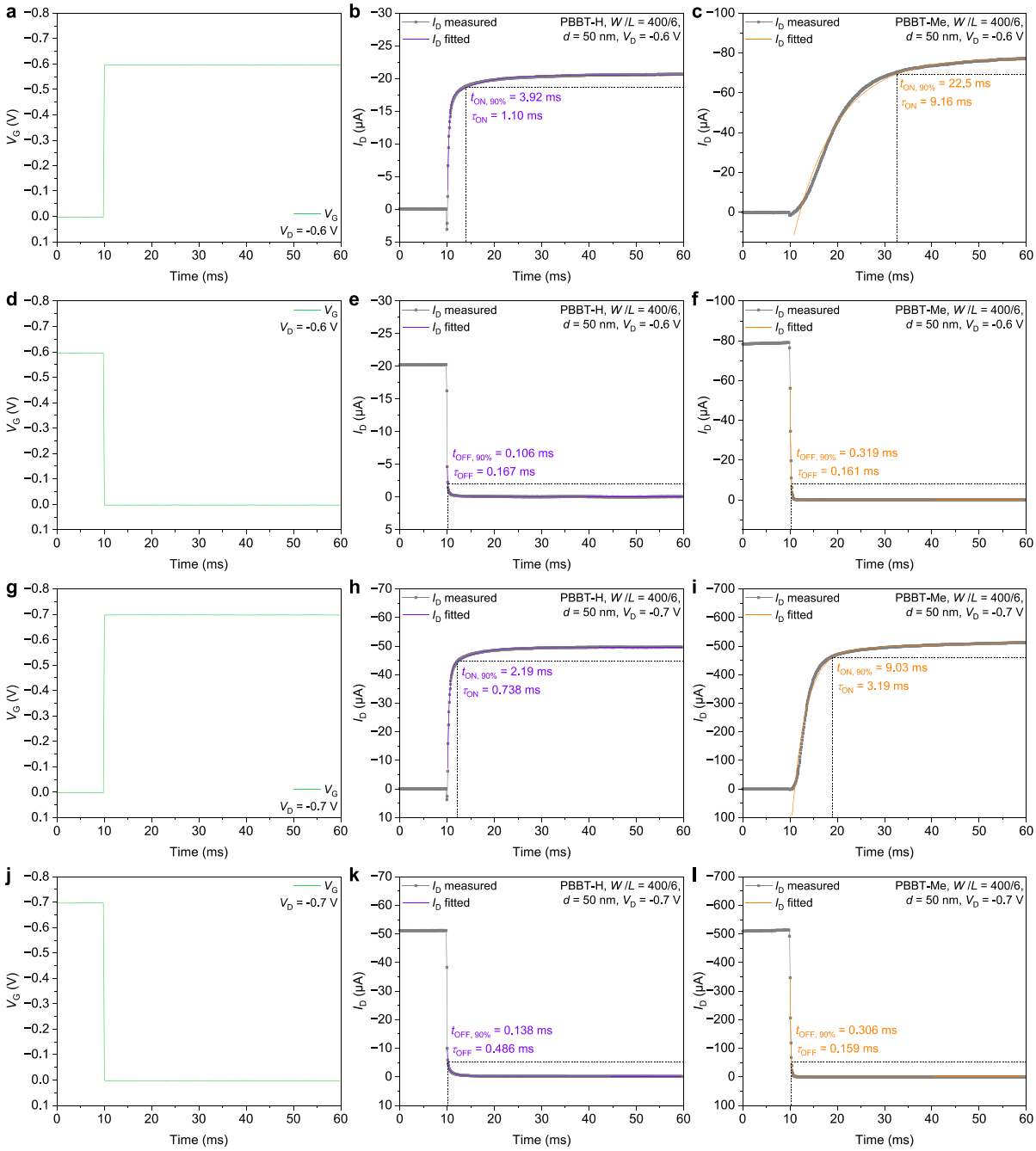

Fig. S13. Transient response of the OECTs: a-c) Gate voltage applied (0 V to -0.6 V, a) and the corresponding τ_{ON} of the OECTs based on PBBT-H (b) and PBBT-Me (c). d-f) Gate voltage applied (-0.6 V to 0 V, d) and the corresponding τ_{OFF} of the OECTs based on PBBT-H (e) and PBBT-Me (f). g-i) Gate voltage applied (0 V to -0.7 V, g) and the corresponding τ_{ON} of the OECTs based on PBBT-H (h) and PBBT-Me (i). j-l) Gate voltage applied (-0.7 V to 0 V, j) and the corresponding τ_{OFF} of the OECTs based on PBBT-H (k) and PBBT-Me (l). Rise time ($t_{ON, 90\%}$) and fall time ($t_{OFF, 90\%}$) of all the OECTs are shown in the figures.

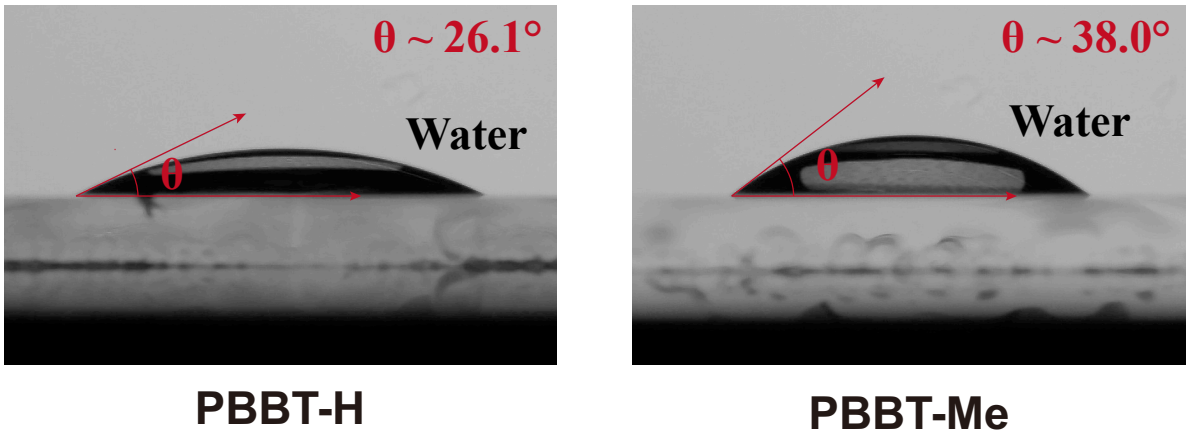

Fig. S14. Contact angles of PBBT-H and PBBT-Me in air.

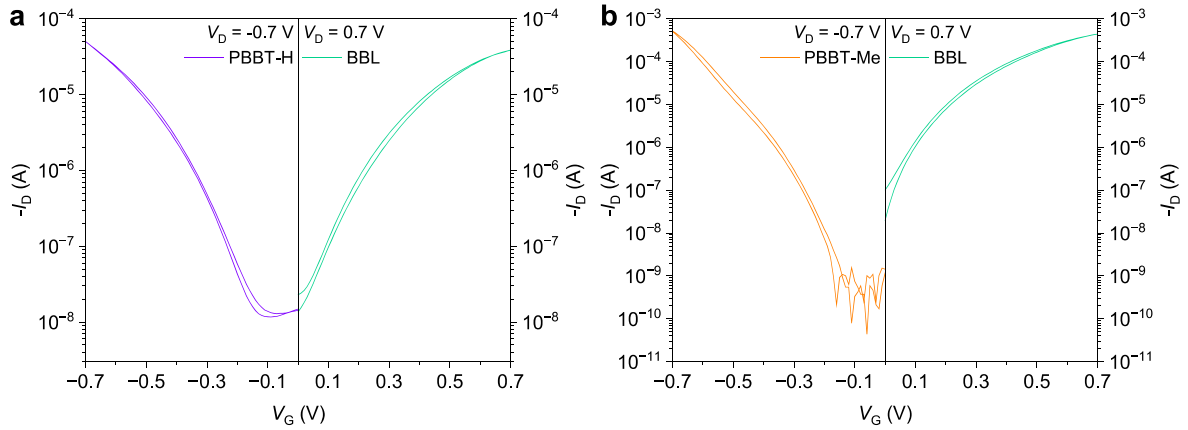

Fig. S15. Transfer curves of the complementary OECTs: a) Transfer curves of PBBT-H-based OECT (p-type) and BBL-based OECT (n-type). b) Transfer curves of PBBT-Me-based OECT (p-type) and BBL-based OECT (n-type).

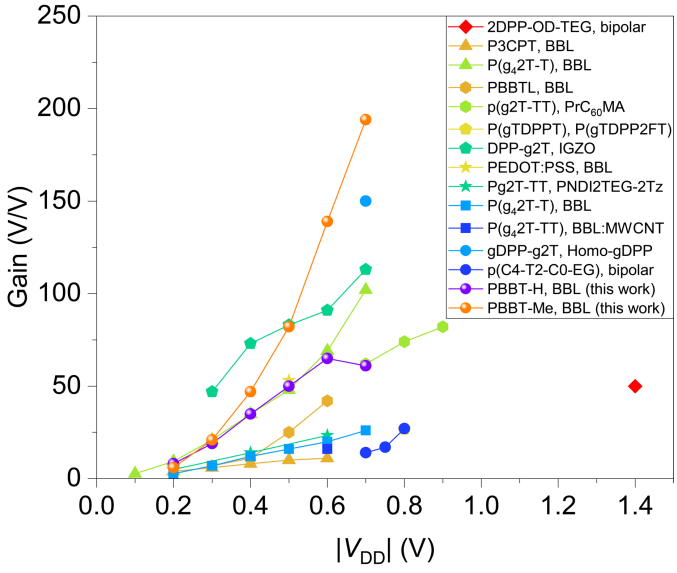

Fig. S16. Summary of V_{DD}-dependent voltage gain of complementary inverters based on OECT.

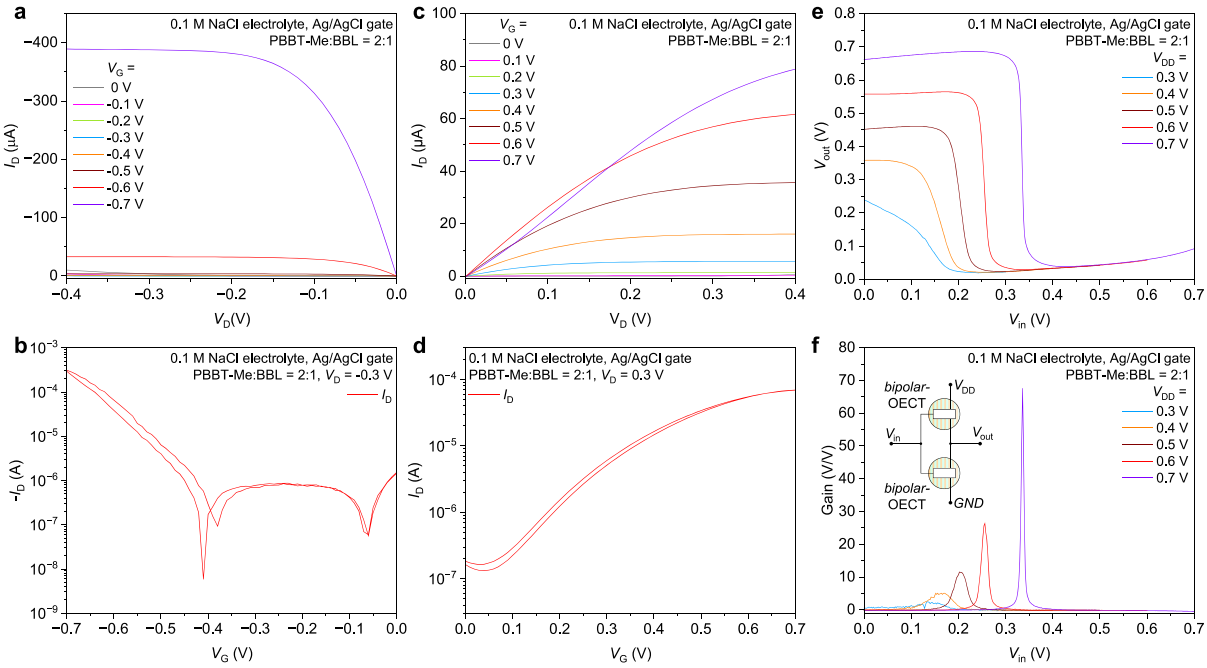

Fig. S17. OECT (a-d) and inverter (e-f) performance based on PBBT-H:BBL blend. The PBBT-H:BBL blend (spin-coated from MSA with a mass ratio of 2:1 PBBT-H:BBL) shows typical ambipolar OECT characteristics. The corresponding complementary OECT inverters show high voltage gains of up to 67 V/V at V_{DD} = 0.7 V.

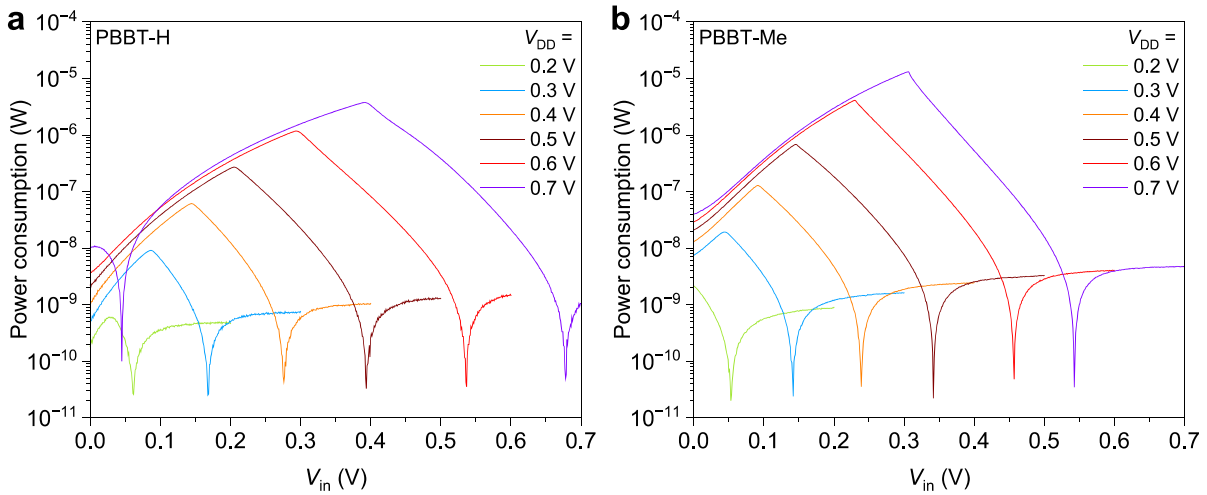

Fig. S18. Power consumption of the complementary inverters (PBBT-H/PBBT-Me based p-type OECT and BBL based n-type OECT): Power consumption of the inverter based on PBBT-H and BBL (a) and the inverter based on PBBT-Me and BBL (b) at various supply voltages.

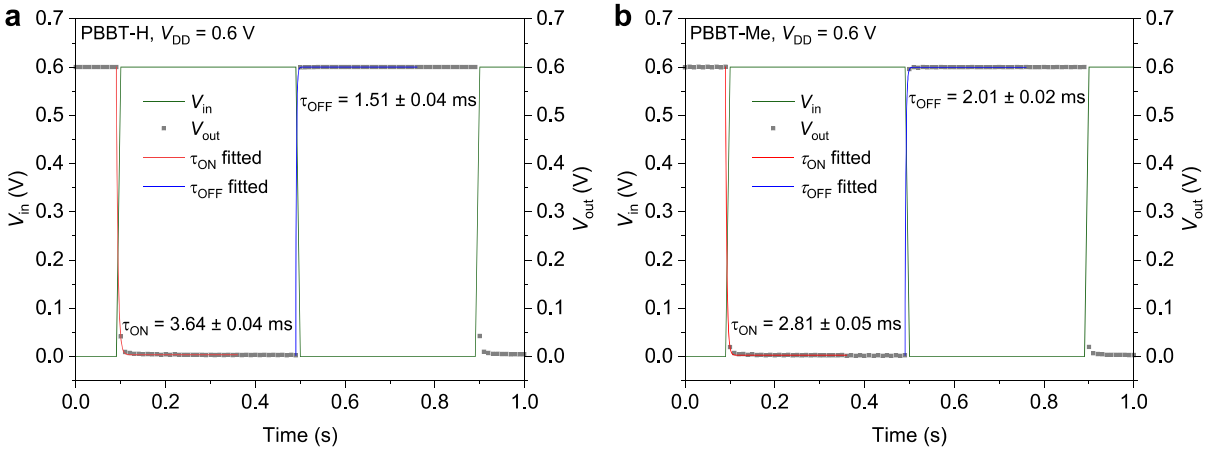

Fig. S19. Transient response of the complementary inverters (PBBT-H/PBBT-Me based p-type OECT and BBL based n-type OECT): Transient response curves of the inverter based on PBBT-H and BBL (a) and the inverter based on PBBT-Me and BBL. τ_{ON} and τ_{OFF} were evaluated through a first-order exponential fitting.

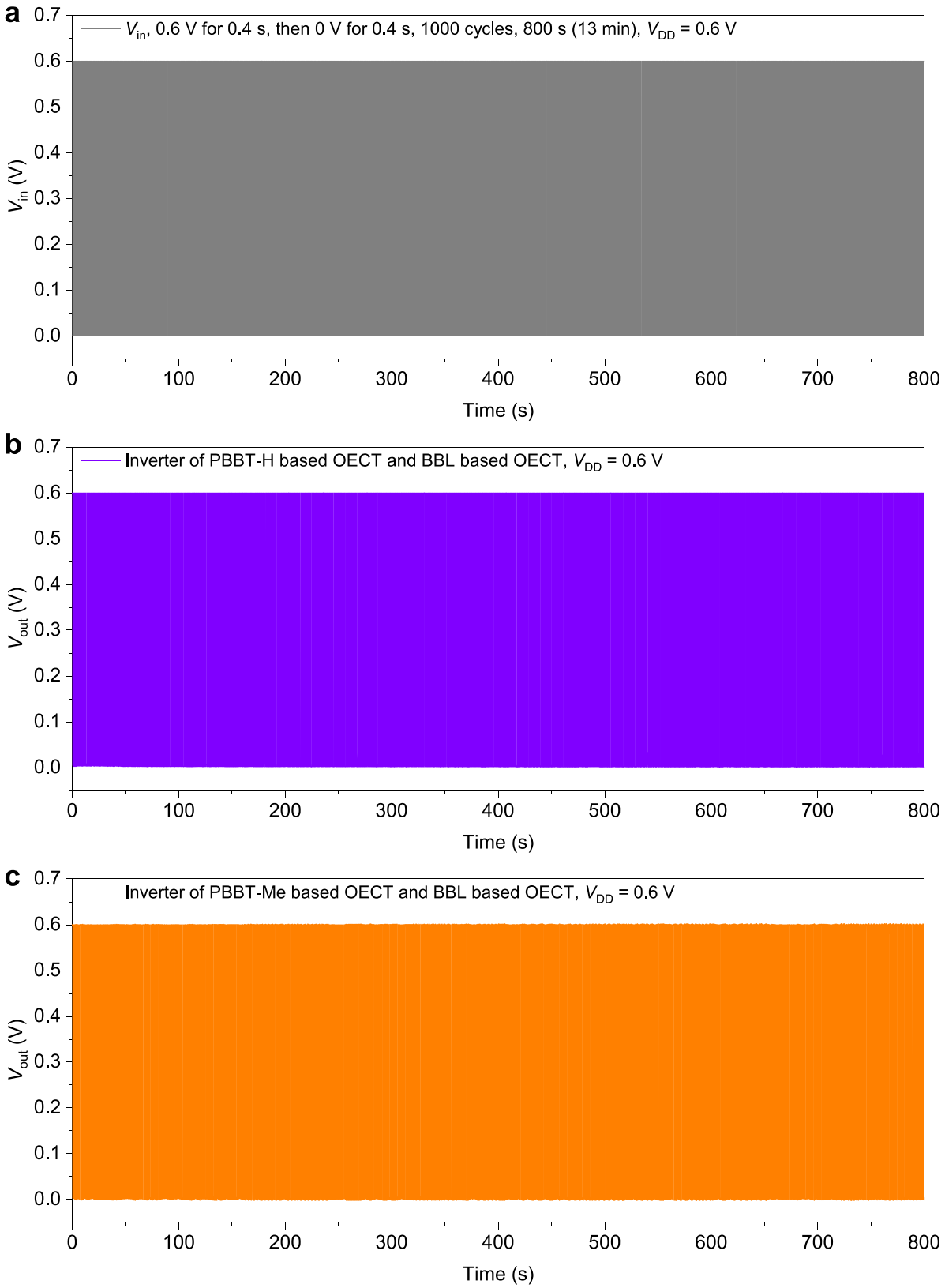

Fig. S20. Stability of the complementary inverters (PBBT-H/PBBT-Me based p-type OECT and BBL based n-type OECT): a) Gate voltage pulses applied to the inverters. b-c) Drain current response of the inverter based on PBBT-H and BBL (b) and the inverter based on PBBT-Me and BBL.

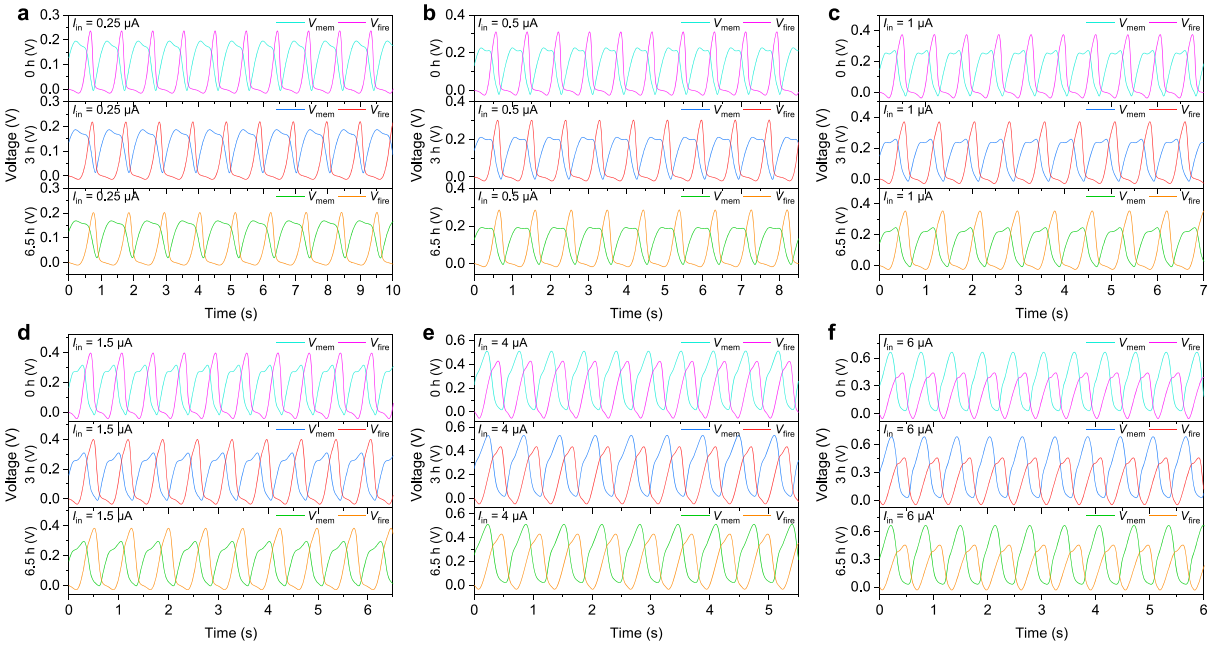

Fig. S21. Spiking waveforms of the LIF neuron after working at I_{in} = 0.25 μA, 0.5 μA, 1 μA, 1.5 μA, 4 μA, 6 μA for 0 h, 3 h, and 6.5 h.

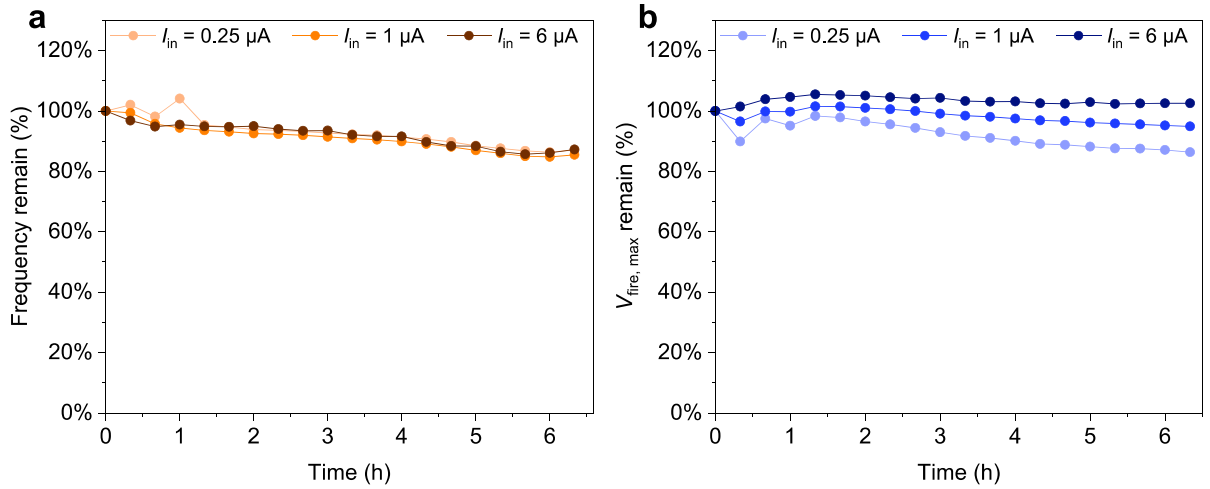

Fig. S22. Frequency (a) and $V_{fire,max}$ (b) change of the LIF neuron at I_{in} = 0.25 μA, 1μA, 6 μA during 6.5 h of continuous operation.

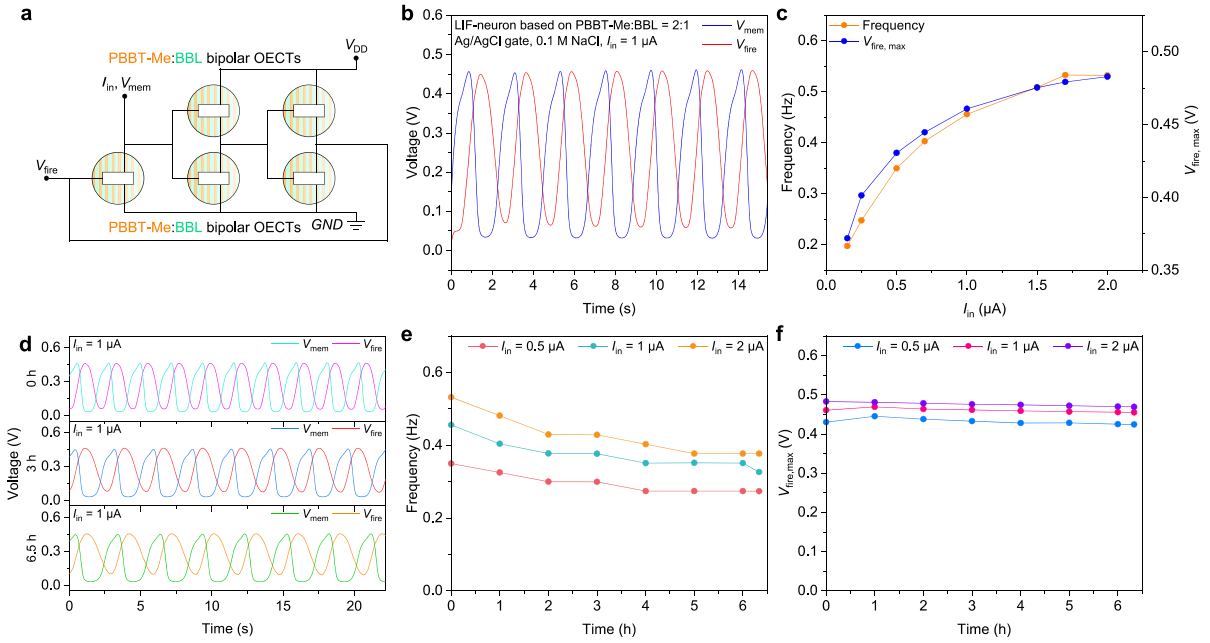

Fig. S23. PBBT-Me: BBL-based OECNs. a) Schematic of LIF type spiking neuron, comprising PBBT-Me:BBL 2:1 blend ambipolar OECTs. b) Typical spiking behaviors of a LIF-neuron at I_{in} = 1 μA. c) Spiking frequency and $V_{fire,max}$ of the LIF-neuron at different I_{in}. d) Spiking patterns at I_{in} = 1 μA for 0 h, 3 h, and 6.5 h. e) Spiking frequencies of the LIF-neuron change over time at I_{in} = 0.5 μA, 1 μA, 2 μA during 6.5 h of continuous operation. f) Evolution of the $V_{fire,max}$ over time at I_{in} = 0.5 μA, 1 μA, 2 μA during 6.5 h of continuous operation.

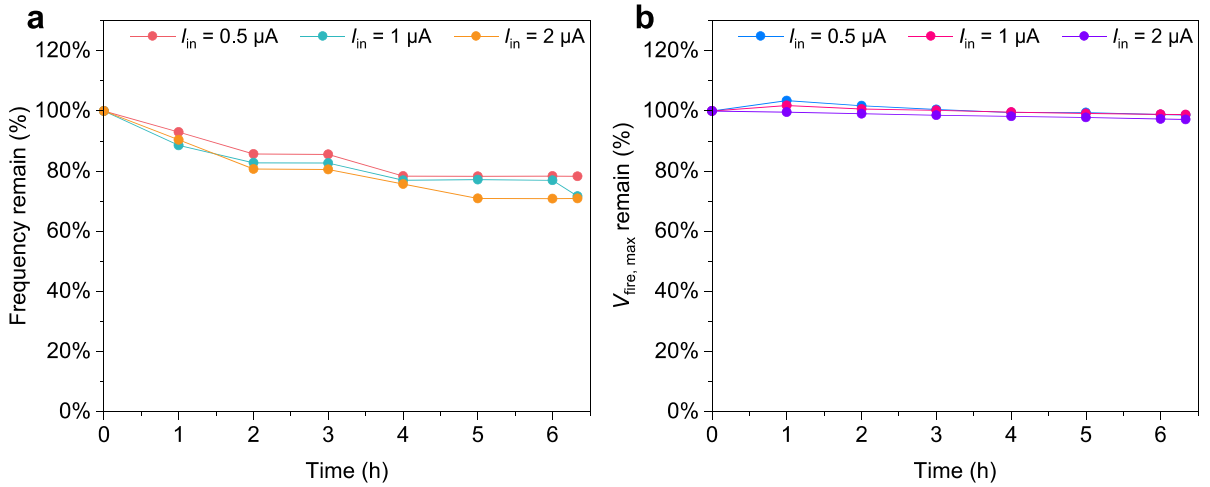

Fig. S24. Frequency (a) and $V_{fire,max}$ (b) change of the LIF neuron at I_{in} = 0.5 μA, 1 μA, 2 μA during 6.5 h of continuous operation.

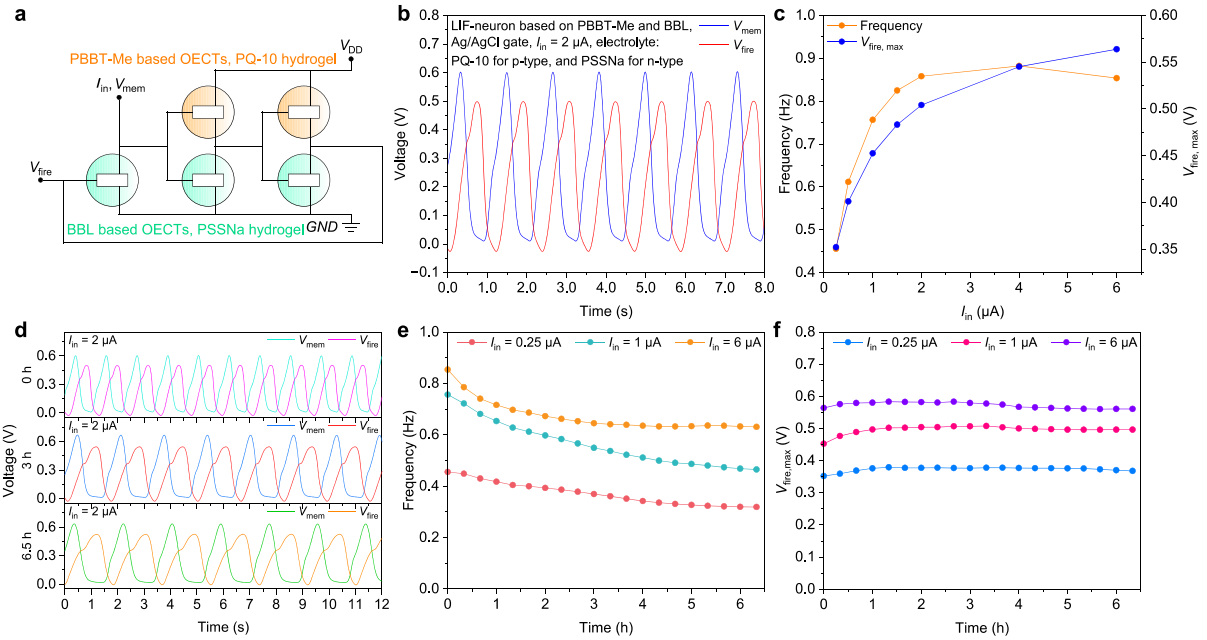

Fig. S25. PBBT-Me and BBL-based OECNs comprising solid hydrogels. a) Schematic of the LIF type spiking neuron, comprising both p-type and n-type accumulation-mode OECTs. b) Typical spiking behaviors of a LIF-neuron at I_{in} = 2 μA, based on PBBT-Me (PQ-10 hydrogel electrolyte[5]) and BBL OECTs (PSSNa hydrogel electrolyte). c) Spiking frequency and $V_{fire,max}$ of the LIF-neuron at different I_{in}. d) Spiking patterns at I_{in} = 2 μA for 0 h, 3 h, and 6.5 h. e) Spiking frequencies of the LIF-neuron change over time at I_{in} = 0.25 μA, 1 μA, 6 μA during 6.5 h of continuous operation. f) Evolution of the $V_{fire,max}$ over time at I_{in} = 0.25 μA, 1 μA, 6 μA during 6.5 h of continuous operation.

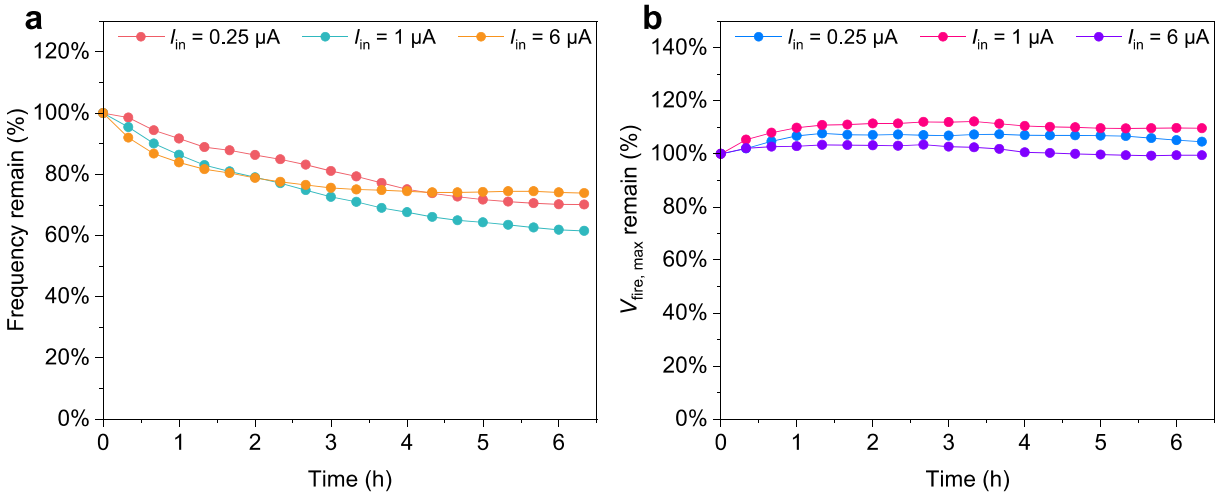

Fig. S26. Frequency (a) and $V_{fire,max}$ (b) change of the LIF neuron (PBBT-Me and BBL OECTs, hydrogel electrolytes, see Fig. S25) at I_{in} = 0.25 μA, 1 μA, 6 μA during 6.5 h of continuous operation.

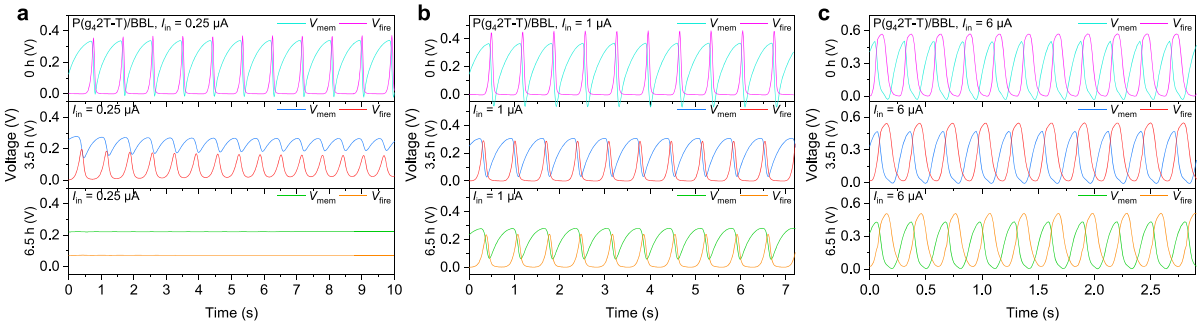

Fig. S27. Spiking waveforms of the LIF neuron based on P(g$_4$2T-T) and BBL, after working continuously at I_{in} = 0.7 μA, 1 μA, 6 μA for 0 h, 3 h, and 6.5 h. For I_{in} < 0.7 μA, the neuron did not show spiking.

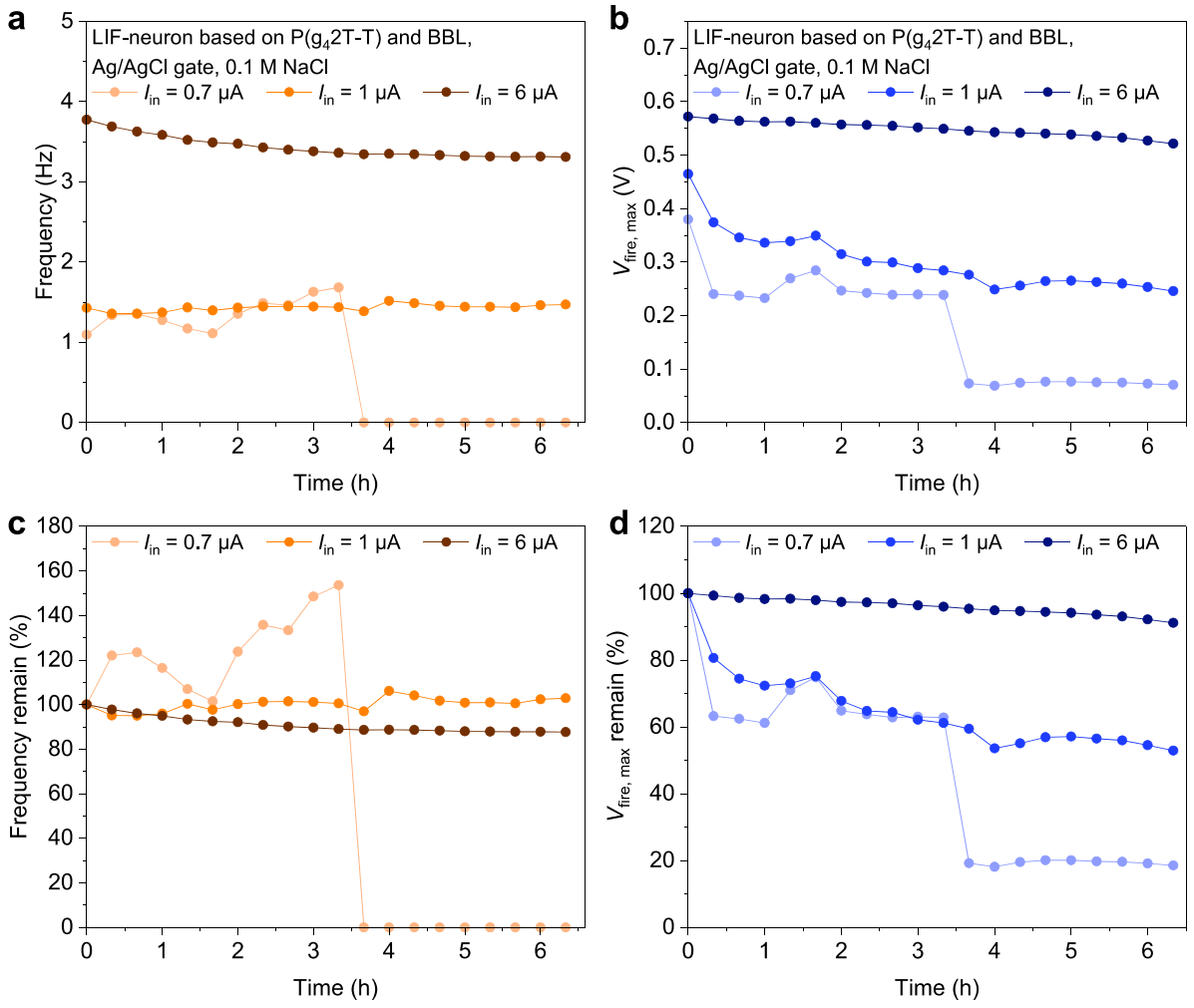

Fig. S28. Frequency (a, c) and $V_{fire,max}$ (b, d) change of LIF neuron based on P(g$_4$2T-T) and BBL, at I_{in} = 0.7 μA, 1μA, 6 μA during 6.5 h of continuous operation.

Table S1. Comparison of p-type, accumulation mode OECT stability under continuous cycling in air with aqueous solution electrolyte.

Compound	Electrolyte	V_D	V_G	Cycling time	Current retention	Reference
P3gCPDT-1gT2	0.1 M NaCl	-0.2 V	0 to -0.6 V	1 h	96%	[6]
P3gCPDT-1gT2	0.1 M NaCl	-0.2 V	0 to -0.6 V	2 h	91%	
P3gCPDT-MeOT2	0.1 M NaCl	-0.2 V	0 to -0.6 V	1 h	98%	
P3gCPDT-MeOT2	0.1 M NaCl	-0.2 V	0 to -0.6 V	2 h	95%	
CB + BCF + p(g3T2-T)[a]	0.1 M NaCl	-0.6 V	0 to -0.6 V	2 h	46%	[7]
P(bgDPP-MeOT2)	0.1 M NaCl	-0.4 V	0 to -0.4 V	30 min[b]	98.8%	[8]
P(bgDPP-MeOT2)	0.1 M NaCl	-0.4 V	0 to -0.4 V	125 min[b]	89%	
p(g2T2-g4T2)	0.1 M NaCl	-0.6 V	0 to -0.6 V	120 min	87%	[9]
p(g1T2-g5T2)	0.1 M NaCl	-0.6 V	0 to -0.6 V	120 min	98%	
p(g0T2-g6T2)	0.1 M NaCl	-0.6 V	0 to -0.6 V	120 min	98%	
p(gPyDPP-MeOT2)	0.1 M NaCl	-0.4 V	0 to -0.5 V	25 min	124% [b]	[10]
p(gPyDPP-MeOT2)	0.1 M NaCl	-0.4 V	0 to -0.6 V	25 min	96% [b]	
p(gPyDPP-MeOT2)	0.1 M NaCl	-0.4 V	0 to -0.7 V	25 min	87% [b]	
PProDOT-DPP	0.1 M $LiPF_6$	-0.1 V	0 to -0.2 V	5 min	121% [b]	[11]
PProDOT-DPP	0.1 M $LiPF_6$	-0.1 V	0 to -0.4 V	5 min	87%[b]	
PProDOT-DPP	0.1 M $LiPF_6$	-0.1 V	0 to -0.6 V	5 min	68%[b]	
PBBT-H	0.1 M NaCl	-0.6 V	0 to -0.6 V	4 h	90%	This work
PBBT-Me	0.1 M NaCl	-0.6 V	0 to -0.6 V	4 h	92%	

Table S2. Summary of V_{DD}-dependent voltage gain of complementary inverters based on OECT.

p-type OECT materials	n-type OECT materials	$\lvert V_{DD}\rvert$ (V)	Gain	Ref.
2DPP-OD-TEG	2DPP-OD-TEG	1.4	50	[12]
P3CPT	BBL	0.2	4	[13]
		0.3	6	
		0.4	8	
		0.5	10	
		0.6	11	
P($g_4$2T-T)	BBL	0.1	2.7	[14]
		0.2	9.4	
		0.3	21	
		0.4	35	
		0.5	48	
		0.6	69	
		0.7	102	
PBBTL	BBL	0.3	7	[1]
		0.4	11	
		0.5	25	
		0.6	42	
p(g2T-TT)	$PrC_{60}MA$	0.7	62	[15]
		0.8	74	
		0.9	82	
P(gTDPPT)	P(gTDPP2FT)	0.8	26.8	[16]
DPP-g2T	IGZO	0.3	47	[17]
		0.4	73	
		0.5	83	
		0.6	91	
		0.7	113	
PEDOT:PSS	BBL	0.5	53	[18]
Pg2T-TT	PNDI2TEG-2Tz	0.2	5	[19]
		0.4	14	
		0.6	23.4	
P($g_4$2T-T)	BBL	0.2	2.7	[5]
		0.3	7	
		0.4	12	
		0.5	16	
		0.6	20	
		0.7	26	
P($g_4$2T-TT)	BBL:MWCNT	0.6	16	[20]
gDPP-g2T	Homo-gDPP	0.7	150	[21]

p(C_4-T_2-C_0-EG)	p(C_4-T_2-C_0-EG)	0.7	14	[22]
		0.75	17	
		0.8	27	
PBBT-H	BBL	0.2	8	This work
		0.3	19	
		0.4	35	
		0.5	50	
		0.6	65	
		0.7	61	
PBBT-Me	BBL	0.2	6	This work
		0.3	21	
		0.4	47	
		0.5	82	
		0.6	139	
		0.7	194	

Reference

1. X. H. Wu, T. L. D. Tam, S. Chen, T. Salim, X. M. Zhao, Z. L. Zhou, M. Lin, J. W. Xu, Y. L. Loo and W. L. Leong, *Adv. Mater.*, 2022, **34**, 2206118.
2. T. L. D. Tam, M. Lin, S. W. Chien and J. W. Xu, *ACS Macro Lett.*, 2022, **11**, 110-115.
3. J. Duan, G. Zhu, L. Lan, J. Chen, X. Zhu, C. Chen, Y. Yu, H. Liao, Z. Li, I. McCulloch and W. Yue, *Angew. Chem. Int. Ed. Engl.*, 2023, **62**, e202213737.
4. R. B. Rashid, A. M. Evans, L. A. Hall, R. R. Dasari, E. K. Roesner, S. R. Marder, D. M. D'Allesandro, W. R. Dichtel and J. Rivnay, *Adv. Mater.*, 2022, **34**, e2110703.
5. C. Y. Yang, D. Tu, T. P. Ruoko, J. Y. Gerasimov, H. Y. Wu, P. C. Harikesh, M. Massetti, M. A. Stoeckel, R. Kroon, C. Muller, M. Berggren and S. Fabiano, *Adv. Electron. Mater.*, 2022, **8**, 2100907.
6. L. Lan, J. Chen, Y. Wang, P. Li, Y. Yu, G. Zhu, Z. Li, T. Lei, W. Yue and I. McCulloch, *Chem. Mater.*, 2022, **34**, 1666.
7. T. C. H. Castillo, M. Moser, C. Cendra, P. D. Nayak, A. Salleo, I. McCulloch and S. Inal, *Chem. Mater.*, 2022, **34**, 6723.
8. H. Y. Jia, Z. Huang, P. Y. Li, S. Zhang, Y. F. Wang, J. Y. Wang, X. D. Gu and T. Lei, *J. Mater. Chem. C*, 2021, **9**, 4927-4934.
9. M. Moser, T. C. Hidalgo, J. Surgailis, J. Gladisch, S. Ghosh, R. Sheelamanthula, Q. Thiburce, A. Giovannitti, A. Salleo, N. Gasparini, A. Wadsworth, I. Zozoulenko, M. Berggren, E. Stavrinidou, S. Inal and I. McCulloch, *Adv. Mater.*, 2020, **32**, 2002748.
10. A. Giovannitti, R. B. Rashid, Q. Thiburce, B. D. Paulsen, C. Cendra, K. Thorley, D. Moia, J. T. Mefford, D. Hanifi, W. Y. Du, M. Moser, A. Salleo, J. Nelson, I. McCulloch and J. Rivnay, *Adv. Mater.*, 2020, **32**, 1908047.
11. X. Y. Luo, H. G. Shen, K. Perera, D. T. Tran, B. W. Boudouris and J. G. Mei, *ACS Macro Lett.*, 2021, **10**, 1061-1067.
12. J. J. Samuel, A. Garudapalli, A. A. Mohapatra, C. Gangadharappa, S. Patil and N. P. B. Aetukuri, *Adv. Funct. Mater.*, 2021, **31**, 2102903.
13. H. D. Sun, M. Vagin, S. H. Wang, X. Crispin, R. Forchheimer, M. Berggren and S. Fabiano, *Adv. Mater.*, 2018, **30**, 1704916.
14. H. Y. Wu, C. Y. Yang, Q. F. Li, N. B. Kolhe, X. Strakosas, M. A. Stoeckel, Z. Wu, W. L. Jin, M. Savvakis, R. Kroon, D. Y. Tu, H. Y. Woo, M. Berggren, S. A. Jenekhe and S. Fabiano, *Adv. Mater.*, 2022, **34**, 2106235.
15. E. Stein, O. Nahor, M. Stolov, V. Freger, I. M. Petruta, I. McCulloch and G. L. Frey, *Nat. Commun.*, 2022, **13**, 5548.
16. P. Y. Li, J. W. Shi, Y. Q. Lei, Z. Huang and T. Lei, *Nat. Commun.*, 2022, **13**, 5970.
17. Y. Yao, W. Huang, J. Chen, G. Wang, H. Chen, X. Zhuang, Y. Ying, J. Ping, T. J. Marks and A. Facchetti, *Proc. Natl. Acad. Sci. U. S. A.*, 2021, **118**, e2111790118.
18. P. Romele, P. Gkoupidenis, D. A. Koutsouras, K. Lieberth, Z. M. Kovacs-Vajna, P. W. M. Blom and F. Torricelli, *Nat. Commun.*, 2020, **11**, 3743.
19. Y. Zhang, G. Ye, T. P. A. van der Pol, J. Dong, E. R. W. van Doremaele, I. Krauhausen, Y. Liu, P. Gkoupidenis, G. Portale, J. Song, R. C. Chiechi and Y. van de Burgt, *Adv. Funct. Mater.*, 2022, **32**, 2201593.
20. S. L. Zhang, M. Massetti, T. P. Ruoko, D. Y. Tu, C. Y. Yang, X. J. Liu, Z. A. Wu, Y. Lee, R. Kroon, P. O. A. Persson, H. Y. Woo, M. Berggren, C. Muller, M. Fahlman and S. Fabiano,

Adv. Funct. Mater., 2022, **32**, 2106447.
21. W. Huang, J. H. Chen, Y. Yao, D. Zheng, X. D. Ji, L. W. Feng, D. Moore, N. R. Glavin, M. Xie, Y. Chen, R. M. Pankow, A. Surendran, Z. Wang, Y. Xia, L. B. Bai, J. Rivnay, J. F. Ping, X. G. Guo, Y. H. Cheng, T. J. Marks and A. Facchetti, *Nature*, 2023, **613**, 496.
22. R. B. Rashid, W. Y. Du, S. Griggs, I. P. Maria, I. McCulloch and J. Rivnay, *Sci. Adv.*, 2021, **7**, eabh1055.